ELSEVIER ELSEVIER

Contents lists available at ScienceDirect

Earth and Planetary Science Letters

www.elsevier.com/locate/epsl



The deep Shumagin gap filled: Kinematic rupture model and slip budget analysis of the 2020 Mw 7.8 Simeonof earthquake constrained by GNSS, global seismic waveforms, and floating InSAR



Zhuohui Xiao ^{a,b}, Jeffrey T. Freymueller ^{b,*}, Ronni Grapenthin ^c, Julie L. Elliott ^{d,1}, Connor Drooff ^b, Logan Fusso ^c

- ^a School of Geodesy and Geomatics, Wuhan University, Wuhan, China
- ^b Dept. of Earth and Environmental Sciences, Michigan State University, East Lansing, MI, United States of America
- ^c Geophysical Institute and Dept. of Geosciences, University of Alaska Fairbanks, Fairbanks, AK, United States of America
- d Dept. of Earth, Atmospheric, and Planetary Sciences, Purdue University, West Lafayette, IN, United States of America

ARTICLE INFO

Article history:

Received 10 June 2021

Received in revised form 4 September 2021

Accepted 4 October 2021 Available online 22 October 2021 Editor: I.P. Avouac

Dataset link:

http://ds.iris.edu/wilber3/find_event

Dataset link: http://www.unavco.org

Dataset link: https://geodesy.noaa.gov/CORS/

Dataset link: https://www.isc.ac.uk/

Dataset link: https://earthquake.usgs.gov/earthquakes/map/

Dataset link:

https://doi.org/10.6084/m9.figshare. 16567470.v1

Keywords:

space-time slip model Shumagin gap floating InSAR slip deficit tsunami hazard

ABSTRACT

On 22 July 2020, the Mw 7.8 Simeonof megathrust earthquake struck offshore of the Alaska Peninsula. This was the largest event since 1917 in the enigmatic area known as the Shumagin seismic gap, a region of transitional plate interface coupling from highly coupled to the east to creeping to the west. Hence, this event provides a rare chance to understand rupture mechanics on such heterogeneously coupled faults. In this study, we examine the rupture process of the 2020 Simeonof earthquake with a combination of static GNSS displacements, InSAR displacements, high-rate GNSS waveforms and teleseismic waveforms. Due to the discontinuous nature of the deformation field, we use InSAR data for individual islands and tie the displacement field either to GNSS observations or keep these "floating", i.e. we estimate an ambiguity parameter during the inversion. Our results demonstrated that the rupture process of this event is unidirectional, initiating at the hypocenter and propagating westward for about 130 s with an average rupture velocity of ∼1.9 km/s. The highest slip was centered below the Koniuji Islands and occurred between 20 s to 50 s after the rupture initiation. We find that InSAR observations, especially "floating" data on near-field islands, provide essential constraints for the slip inversion, building confidence in the slipping of the less coupled region. Comparison with an existing and an alternative plate coupling model demonstrated that the remaining slip budget is unlikely to be able to generate a large event at depths from 30 to 40 km, as the Shumagin seismic gap has been mostly filled by the 2020 Simeonof earthquake at those depths. However, both coupling models suggest a substantial slip deficit in shallow near trench regions, suggesting that a significant earthquake can still occur. Seafloor geodetic observations are required to further constrain the near-trench plate coupling.

© 2021 Elsevier B.V. All rights reserved.

1. Introduction

The Alaska-Aleutian subduction zone, where the Pacific plate subducts beneath the North American plate at a rate of 60-70 mm/yr (Argus et al., 2010), has been struck by several great (M>8) earthquakes since the beginning of the 20th century (Fig. 1). The

region between the 1938 Mw 8.3 and 1946 M_S 7.4 earthquake ruptures was identified as a seismic gap (hereafter Shumagin gap; Davies et al., 1981), which had not ruptured since an Mw 7.4 event in 1917 (Estabrook and Boyd, 1992). The seismicity catalog from the International Seismological Center (ISC, Storchak et al., 2020) covering the last 50 years indicates a lack of significant seismic activity (Mw \geq 3) in the shallower plate interface within the Shumagin gap (Fig. 1). Global Navigation Satellite System (GNSS) observations over the last two decades imply variable degrees of slip deficit along the subduction interface (e.g., Drooff and Freymueller, 2021; Li and Freymueller, 2018). Slip deficit estimates range from

^{*} Corresponding author.

E-mail address: freymuel@msu.edu (J.T. Freymueller).

¹ Now at Department of Earth and Environmental Sciences, Michigan State University

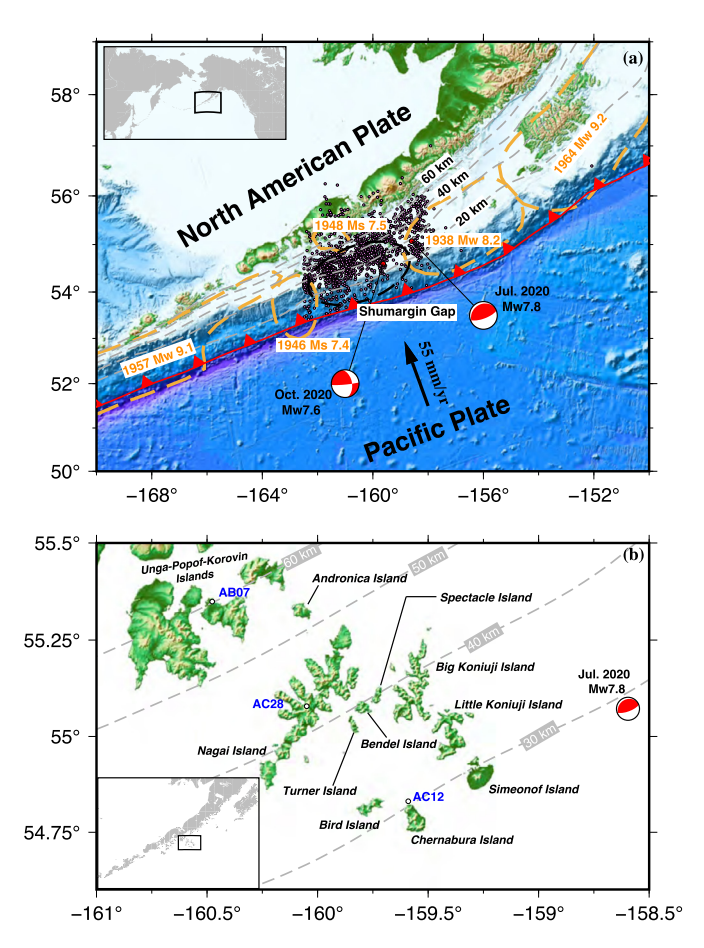


Fig. 1. (a) Map of the study area and regional plate tectonic setting. Orange lines outline asperities of the Aleutian Megathrust that ruptured in past large earthquakes. Solid purple dots show earthquakes (Mw ≥ 3) from January 1970 to July 2020. The seismicity catalog is from International Seismological Centre On-line Bulletin (https://doi.org/10.31905/D808B830). The annotated hatched gray lines are depth contours from the Slab 2.0 (Hayes et al., 2018) model. The black dotted outline indicates the inferred Shumagin Seismic Gap that partially ruptured during the 2020 Simeonof earthquake sequence, locations and mechanisms of the mainshock and largest aftershock are shown. Inset shows the location of the main map within the Aleutian Islands, Alaska. The Pacific plate velocity relative to the Peninsula block (Li et al., 2016) is shown offshore. (b) Shumagin Islands and the three near field GNSS stations (white circles). Note that Bendel and Turner Islands are not covered by the Sentinel-1 InSAR frames. The beachball shows USGS location and focal mechanism of the 2020 Simeonof earthquake. The gray lines are the same as Fig. 1a. Inset shows the location of the main map within the Alaska peninsula. (For interpretation of the colors in the figure(s), the reader is referred to the web version of this

fully locked beneath Kodiak Island to creeping near Sanak Island to the west (Drooff and Freymueller, 2021). Slip deficit within the Shumagin segment is moderate to low. Based on the geodetic interseismic model and assuming the 1917 earthquake was the last significant rupture, the Shumagin gap is capable of producing a Mw 8.1 earthquake (Drooff and Freymueller, 2021).

On 22 July 2020 at 06:12:44 UTC (USGS solution), an Mw 7.8 earthquake (hereafter the Simeonof earthquake) nucleated east of the Shumagin gap. The epicenter falls right along the western border of the 1938 earthquake rupture area (Fig. 1). This event generated a small tsunami of wave amplitude \sim 50 cm observed at the Sand Point tide gauge north of the Shumagin Islands and \sim 15 cm at the open ocean buoy in the Pacific Ocean (Herman and Furlong, 2021).

Prior slip models for the Simeonof event have been inferred from high-rate GNSS and strong motion data (Crowell and Melgar, 2020), a joint inversion of static GNSS, strong motion, and regional and global broadband seismic data (Liu et al., 2020), and

a joint inversion of static GNSS and teleseismic data (Ye et al., 2021). These models all placed the bulk of the slip at depths between 15-40 km to the west of the epicenter, with maximum slip beneath the eastern Shumagin Islands. However, there are important differences between the models. Crowell and Melgar (2020) presented a model with peak slip of 2.0 m released in a single coherent patch almost exclusively west of the epicenter, at a depth of \sim 30 km underneath and just west of Simeonof Island. Liu et al. (2020) presented a more complex model with significant slip near the epicenter, maximum slip of up to 3.2 m under the eastern Shumagin Islands with peak slip underneath the southern tip of Little Koniuji Island at 35 km depth, and another patch of medium slip that ruptured deeper into the Shumagin gap to the west between about 30-35 km depth. The Ye et al. (2021) model consisted of two large slip patches, one near the epicenter and another located under the Shumagin Islands but with a peak slip of almost 3.8 m at a depth of \sim 36 km. Notably, none of these models infer slip in the region near the trench.

Interferometric Synthetic Aperture Radar (InSAR) observations, while complicated by the discontinuous landmasses near the epicenter, provide a powerful tool to address the limited spatial GNSS coverage. As the islands closest to the epicenter are not instrumented with GNSS, only InSAR can constrain the spatial extent of the rupture and slip distribution. Given the transitional nature of plate interface coupling in this region, it is critical to precisely characterize this event to understand the rupture mechanisms in heterogeneously coupled regions, assess the remaining seismic potential in the Shumagin gap, and precisely determine the stress changes induced by the mainshock such as its relation to the October 2020 Mw7.6 Sandpoint aftershock (Herman and Furlong, 2021).

We present a time-dependent finite fault slip model for the 2020 Mw7.8 Simeonof earthquake based on an inversion method that integrates static GNSS displacements, high-rate GNSS-inferred waveforms, global seismic waveforms, and InSAR line-of-sight (LOS) displacements. Using InSAR to constrain the rupture model for this earthquake poses a challenge as most of the deformation occurred across the Shumagin Islands, preventing the unwrapping of the phase information into one single LOS displacement field. Instead, we unwrapped the phase for each island separately, producing several unconnected patches of coherent phase, each patch having a separate ambiguity parameter needed to infer the missing phase cycles. For patches that contained a GNSS site, we tied the InSAR LOS phase to match the GNSS coseismic displacement, creating an absolute coseismic and early postseismic LOS deformation field for the respective islands. We estimated an ambiguity parameter for each remaining unconstrained or "floating" island in the inversion step to infer the missing phase cycles; in effect, this requires the model to match the displacement gradients on these islands. As such, we present the first slip model for this earthquake that is constrained by all available seismic and geodetic data. We find that the InSAR observations, especially the floating InSAR data on near-field islands, are essential to constrain the slip distribution as precisely as possible. Our model shows that only a small portion of the slip deficit inferred by Drooff and Freymueller (2021) has been fully released, focused on the peak slip region, either leaving the potential for future large earthquakes in shallow portions of the interface, or suggesting alternative plate interface coupling models which we explore in this paper.

2. Data and methods

2.1. Data

We selected 48 P and 21 SH global seismic waveforms from stations with good azimuthal coverage, between 30° to 90° epicentral distance, and high signal-to-noise ratios (Fig. S1). We fil-

tered the raw waveforms between 0.001 and 5 Hz to remove high-frequency noise and periodic disturbances and then converted them to ground displacements with a narrower bandpass filter of 0.01 to 1 Hz to suppress noise further. Finally, we resampled all waveforms to 5 samples per second (sps) for computational efficiency.

Static GNSS displacements (Fig. S6) were estimated for each site individually, by fitting the time series of daily positions for two years before and three months after the earthquake (details in Supplementary Text S1). We fit each time series by estimating a linear trend, annual and semi-annual seasonal variations, the coseismic offset at the time of the event, and a logarithmic postseismic relaxation with a relaxation time of 0.025 years (\sim 9 days). We did not account for temporal correlations in the data noise, but scaled the uncertainties so that the reduced chi square statistic for each station's fit was equal to 1.0. This allows us to compute consistent displacement estimates for any epoch following the earthquake. We used the estimated coseismic step offsets in the inversion, and used the displacements at the time of each post-earthquake InSAR image to provide an absolute reference displacement. We used 1 sps data to generate high-rate GNSS time series with GipsyX (Bertiger et al., 2020) rotated into a local east-north-vertical coordinate system (details in Supplementary Text S2). To reduce high frequency noise, we apply a second-order lowpass filter with a 0.4 Hz cut-off frequency to the resulting waveforms. Since horizontal components have better precision than the vertical, we set the weights between horizontal and vertical waveforms to be 3:1 in the inversion.

We use GMTSAR (Sandwell et al., 2011) for two-pass processing of descending Sentinel-1 acquisitions on path 102 frame 407 on 2020-07-12 and 2020-07-24, and path 73 frame 407 on 2020-06-28 and 2020-07-22 (acquired 17:04:27 UTC). Phase coherence is excellent, but we are left with a number of irregular patches of continuous phase for each island or closely linked island group, separated by water. We used SNAPHU (Chen and Zebker, 2002) to unwrap and generate LOS displacement fields for each patch separately. Each separate patch is thus "floating", with an unknown phase difference between any pair of patches.

Because Chernabura, Nagai, and Popof Islands have continuous GNSS sites located on them (Fig. 1b), we projected the GNSSinferred coseismic and postseismic deformation up until the acquisition day of the repeat SAR acquisition into the line of sight of the satellite and adjusted the InSAR LOS deformation for the patches containing those sites to agree with the GNSS displacements at that location. Unwrapping some groups of islands as a single patch worked for Unga, Popof and Korovin Islands, but not for Big and Little Koniuji Islands (despite the rather continuouslooking phase). For each separate patch of InSAR data that could not be connected to a GNSS site after unwrapping, we estimated a phase ambiguity parameter in the slip inversion. We downsampled the LOS observations with a uniform sampling algorithm, generating a total of 1978 and 2183 data points from the absolute and floating InSAR data, respectively. Supplementary Table S1 summarizes how each island was included in the inversion.

2.2. Data weighting

We tested different scenarios to determine the weighting of each data source in the joint inversion (Fig. S2). To optimally weight static GNSS and InSAR data, we inverted only these two data sets, keeping the weight of InSAR observations fixed at 1 and varying the weight of the GNSS data. As we increased the GNSS weight, the root mean square error (RMSE) of GNSS residuals decreased gradually. The RMSE reached 2.5 mm, which is similar to the GNSS accuracy, at a weight of 120:1 for GNSS relative to InSAR (reasonable as the number of InSAR data is \sim 100 times the

number of GNSS data). As the RMSE of InSAR residuals varies only between 4.7 and 5.2 mm, we consider the GNSS weight of 120:1 relative to InSAR acceptable. We employed similar searches to find the optimal weights between seismic and high-rate GNSS waveforms, and all static geodetic data and whole waveforms. Our respective preferred weights are 1:1 and 3:1 (Fig. S2).

2.3. Rupture geometry, model parameters, and inversion method

We constructed a rectangular fault plane that best matched the Slab2.0 (Hayes et al., 2018) interface ranging from 10 to 50 km depth. As a result, the strike of the fault plane is not exactly trench-parallel and the dip represents a depth-averaged dip angle.

Since location errors on offshore earthquakes can easily be several km or more, we tested several candidate locations around the published USGS hypocenter (Fig. S3). In every test, the fault plane went through the hypocenter candidate, was extended to 300 km length and 160 km width, assumed the best matching Slab2.0 dip and strike angles, and then divided into 480 10 km $\times 10$ km patches. The resulting strike and dip angles are 244.3° and 14.5° for the entire fault plane. Green's functions on every subfault were calculated with a 1-D layered regional velocity structure from the LITHO 1.0 model (Pasyanos et al., 2014). We found the best overall fit to the data at a relocated hypocenter (54.922° N, 158.671° W) ~ 17.4 km to the southwest of USGS's epicenter, at 25.4 km depth. This hypocenter shift is within the range of typical earthquake location errors in subduction zones (e.g., Font et al., 2013). The static displacement residuals were reduced by 8% and the waveform residuals are reduced by about 2% by shifting the hypocenter, and the estimated rupture velocity became less heterogeneous. The adjusted hypocenter makes the static displacements and the waveforms more compatible.

With this fault geometry, we estimated the optimal kinematic slip model using a nonlinear algorithm defined in the wavelet domain (Ji et al., 2002), which we extended to estimate ambiguity parameters for floating InSAR patches. We randomly select a reference pixel, for which we estimate an ambiguity parameter to determine its absolute displacement. The relative displacements between reference and all other pixels in the patch constrain the slip model.

For each subfault we simultaneously estimate rupture initiation time, slip amplitude, rake angle, and the shape of an asymmetric rise time function (Ji et al., 2003; Shao et al., 2011). The rupture velocity of each patch could vary spatially between 1.0 km/s and 3.5 km/s. The total slip amplitude on every subfault was constrained to between 0 to 5 m; rake angles ranged from 30° to 150° with an interval of 3°. The start and end times of the asymmetric rise time function were searched from 0 to 10 s in 1 s intervals. The value of the rise time for each subfault was therefore limited to 0 to 20 s.

Because of the intrinsic parameter trade-offs, for instance, between slip position and amplitude, and start of rise time function and rupture initiation, we imposed spatial Laplacian smoothing on the slip amplitude to avoid unphysical slip oscillations and temporal Laplacian smoothing on rupture initiation time variations to compress the roughness of the rupture front. The final slip distribution and model misfit were clearly affected by the regularization factor. To determine the optimal spatial and temporal regularization coefficients, we assess the tradeoff between model misfit and model roughness for both slip model and rupture initiation model (Fig. S4) by finding the regularization parameter that maximizes the curvature of the tradeoff curve, or L-curve (e.g., Aster et al., 2018). Varying this parameter allowed us to produce a family of slip models that vary in roughness (Movie S1), representing the full suite of possible solutions, with our preferred model discussed below. We also evaluated model resolution using a set of simulated

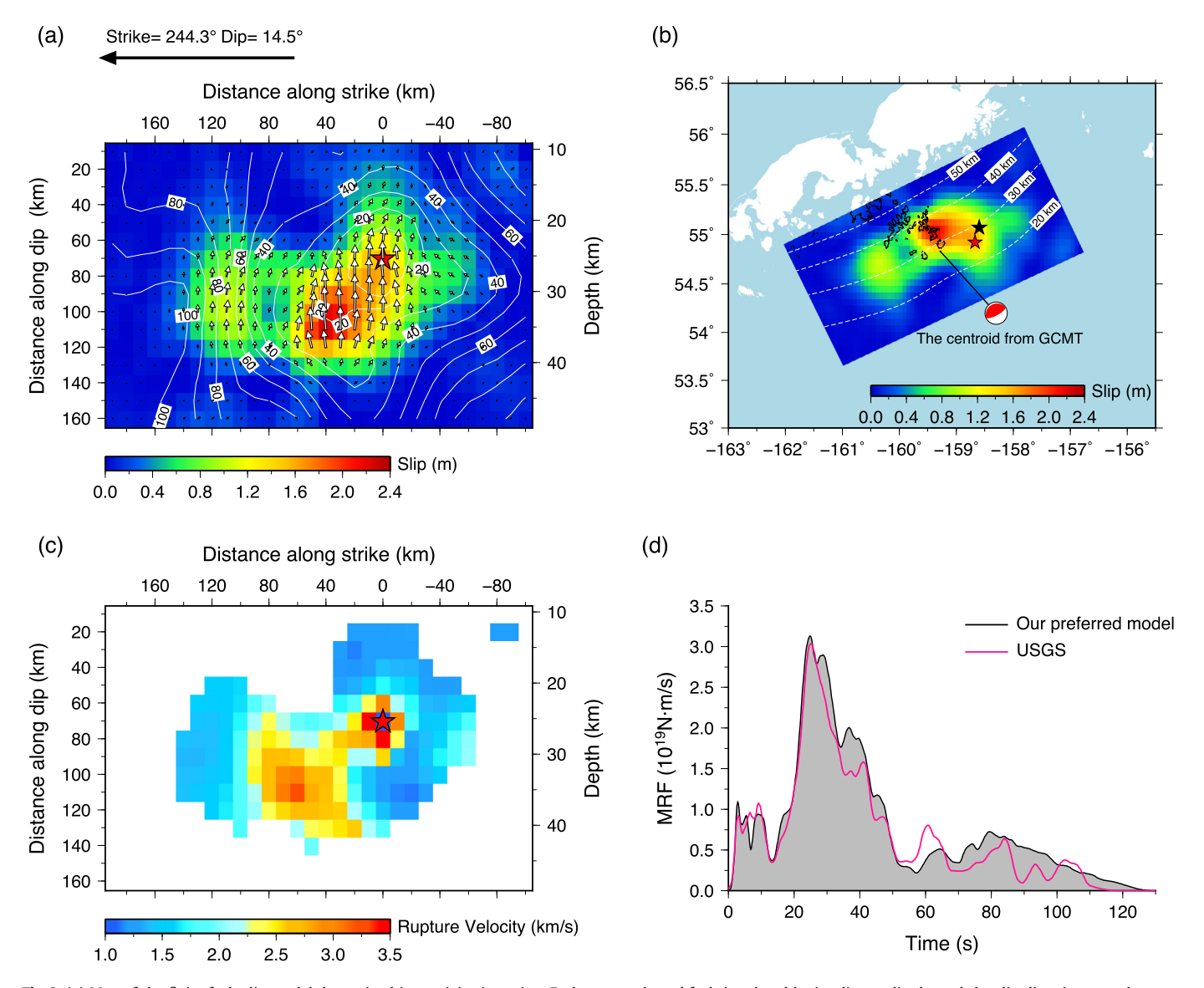


Fig. 2. (a) Map of the finite fault slip model determined in our joint inversion. Each rectangular subfault is colored by its slip amplitude, and the slip directions are shown as scaled arrows in every subfault. The red star indicates the relocated epicenter. The white solid contours display the rupture front location in seconds after the origin time. (b) Slip model projected into map view. The annotated white lines are depth contours from the Slab 2.0 model (Hayes et al., 2018). The black star is the USGS epicenter location. Others are the same as panel (a). (c) Slip rupture velocity for subfaults with slip larger than 30 cm. (d) The moment rate functions of the mainshock predicted by our preferred model (black lines) and USGS (pink lines).

input models (Text S3 and Figure S12). Model resolution using the full data set is poor at shallow depth, but good overall for features in the slip distribution located at 25–40 km depth.

Movie S1 helps to explore how regularization affects the nature of the slip model. The shape and to some extent the location and area of the main slip patch vary considerably as smoothing is changed. Smoother models result in a generally oval-shaped slip patch that extends considerably westward of the along-strike boundary into regions of lower interseismic slip deficit. In rougher models, including our preferred slip model, the edge of the main slip patch is more closely aligned with the boundary between higher and lower plate coupling. Notably, all models regardless of regularization constraints show some slip west of this boundary.

3. Spatio-temporal slip model

Our preferred coseismic slip model for the Mw 7.8 Simeonof Earthquake (Fig. 2) suggests a rupture area of about 170 km along strike and 80 km along dip of the fault interface, characterized by unidirectional rupture westwards from the hypocenter toward the

Shumagin Islands. The rupture propagated from the ${\sim}25$ km depth of the relocated hypocenter down to depths between 30–40 km, where the main slip was released below and east of Big and Little Koniuji Islands. We estimate ${\sim}2.2$ m peak slip at a depth of ${\sim}35$ km to the west-northwest of our relocated hypocenter. Near the hypocenter the slip remained less than 1.5 m. No significant slip (${\geq}0.3$ m) occurred at depths shallower than 15 km. The estimated seismic moment released in this event is 1.01×10^{21} N · m, corresponding to Mw 7.93.

The rupture velocities on subfaults with slip amplitude larger than 30 cm range between 1–3.5 km/s (Fig. 2c). The average velocity of the whole rupture is \sim 1.9 km/s. However, we identify two regions with significantly faster velocities of between 3–3.5 km/s: one located around the hypocenter, and one located deeper at 30–40 km mostly to the west of the peak slip. From the hypocenter, the rupture propagated outward at \sim 3.2 km/s. The average rupture velocity of the deeper fast rupture zone is \sim 2.7 km/s. Notably, this deeper fast slip region overlaps only partially with the peak slip asperity. For about 20–30 km along strike (to the southwest in map view, Fig. 2b) we find velocities larger than 3.0 km/s

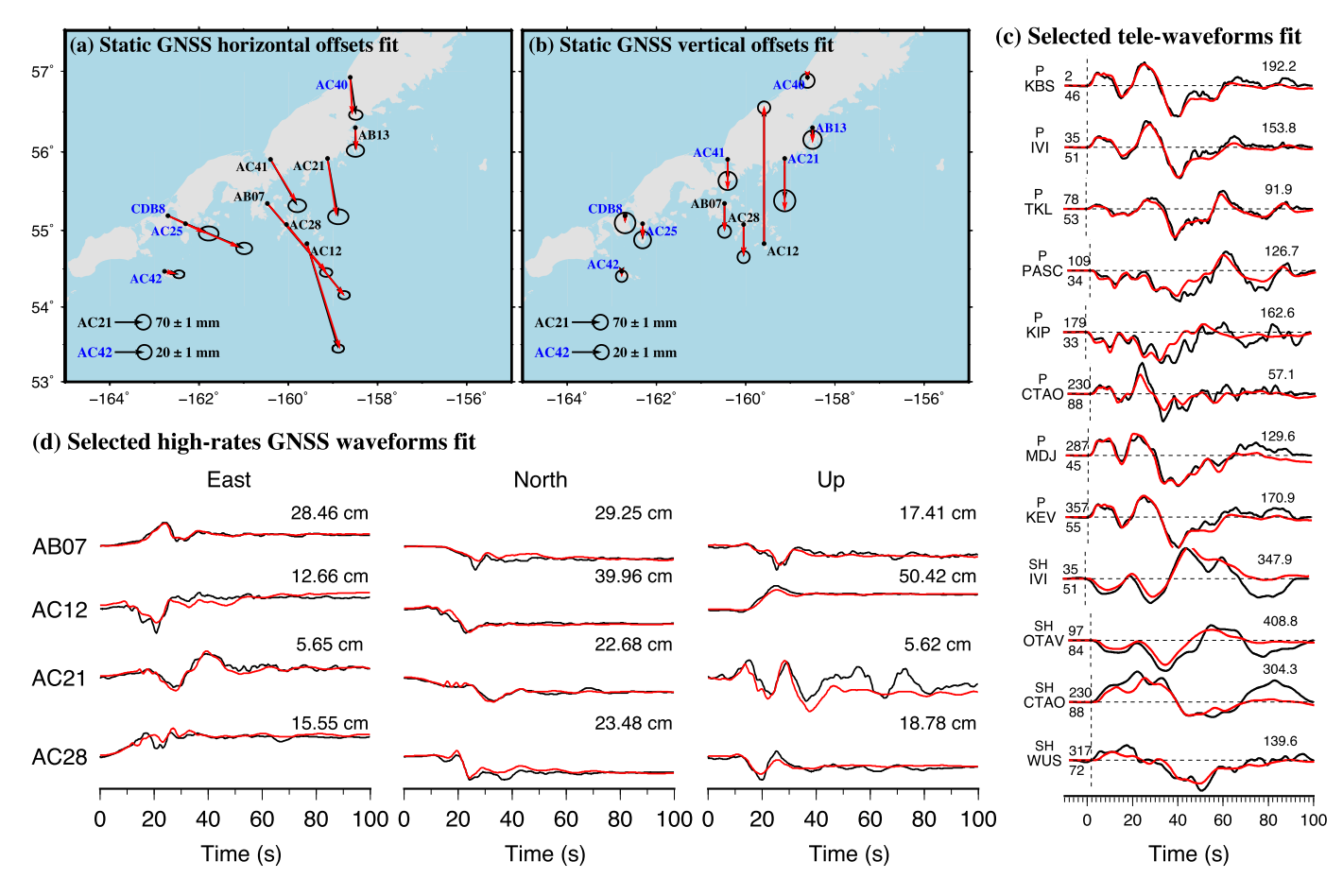


Fig. 3. Fit of static GNSS offsets and selected waveforms. Static GNSS horizontal (a) and vertical (b) offset fits. The Black and red arrows indicate the observations and predictions, respectively. The confidence ellipses indicate 1-sigma data uncertainty. Note the different arrow scales of blue (far field) and black (near field) station names. (c) some selected teleseismic waveforms (black) compared to our model predictions (red), observations and synthetics are aligned by the first P arrivals. At the start of each record we show the type of seismic wave (top left), station name (bottom left), azimuth (top right) and epicenter distance (bottom right, in degrees) for each seismograph. At the end of each record the peak displacement in micrometers is shown. (d) GNSS waveform fits at the four nearest stations. The peak ground displacement is labeled in cm, rest is the same as in (c).

within a region of less than 1 m of slip (compare Figs. 2a and 2c). The average coseismic slip of the whole deeper fast rupture zone is about 1.1 m, only about 50% of the peak slip.

Our inferred moment rate function is very similar to that from the USGS (Fig. 2d) and indicates that the rupture process lasted for about 120 s. Snapshots of the rupture front propagation and slip release are shown in Fig. S5 and Movie S2. We identify three significant pulses in moment release. In the first 10 s, the rupture originated at the hypocenter and propagated outward rapidly, producing the first peak in moment release. From 20 s to 50 s, a much larger pulse of energy was released. The moment rate function increased sharply and reached the second peak at 30 s at which the peak slip at depths of between 30–40 km had been released, followed by a decrease until about 50 s. After that, the rupture propagated unidirectionally along strike and to the west of the epicenter, rupturing to the west of the Shumagin Islands at 25–40 km depth from about 60 s to 120 s with a broad moment release peak centered about 80 s after rupture initiation.

3.1. Model fit to data

Our preferred model predicts the observed coseismic GNSS displacements (Figs. 3a, 3b, S6), teleseismic waveforms (Figs. 3c, S7), and high-rate GNSS waveforms (Figs. 3d, S8) well. Nearly all of the static GNSS horizontal residuals are smaller than 5 mm, except 9.2 mm at site AC41. The vertical GNSS offsets are equally well predicted. The largest vertical residual is 7 mm at site AC21 (\sim 25%

of coseismic offset, within 3-sigma data uncertainties). The RMSE of the static GNSS horizontal and vertical residuals are 2.8 mm and 3.4 mm, respectively, which are on the same order as the observation accuracy. Some notable misfits in the codas of vertical components of some high-rate GNSS waveforms for data with relatively lower signal-to-noise ratios are likely due to site specific effects (e.g., AC21 sits on a bluff near a broad sedimentary valley).

The InSAR data, including the floating observations, are also well fit by our preferred model (Fig. 4). The RMSEs of the absolute and floating data sets are 0.45 cm and 0.60 cm, respectively (see Table S1 for RMSE of individual islands). Predicted phase and LOS deformation (Figs. 4b, 4e) reproduce the main features and gradients of the observed phase and LOS deformation (Figs. 4a, 4d). Obviously, small scale noise such as atmospheric effects are not reproduced and make up most of the misfit (Figs. 4c, 4f) which is in the range of ± 1.5 cm for most of the LOS deformation. Some poorly fitting areas on Big Koniuji Island are of note, but may be due to unwrapping errors as they fall near small land bridges (Fig. 4a).

Based on the good fit to multiple data types, we believe that our preferred model provides a reasonable representation of the rupture process and coseismic slip model. The static GNSS and In-SAR data provide strong constraints on the location of slip, and the high-rate GNSS waveforms provide complementary space and time constraints. The teleseismic waveform data strongly constrain the timing of the slip, but provide little information about its location. Variations in rupture velocity within the overall rupture were re-

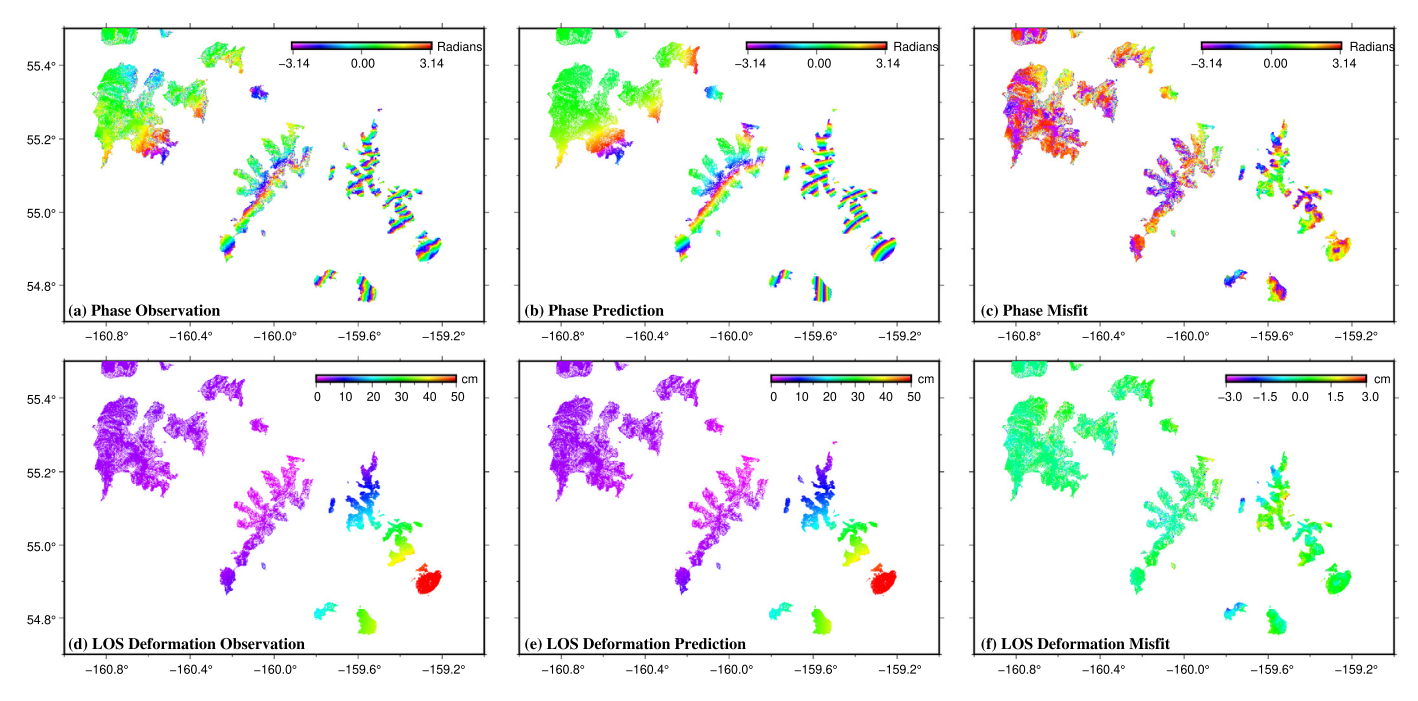


Fig. 4. Comparison of InSAR observations and synthetic deformation derived from our preferred model. (a), (b), (c) are phase observation, phase prediction and phase misfit, respectively. (d), (e), (f) are the LOS deformation observation ("floating" islands have the estimated phase ambiguity added, Table S1), LOS deformation prediction and LOS misfit, respectively.

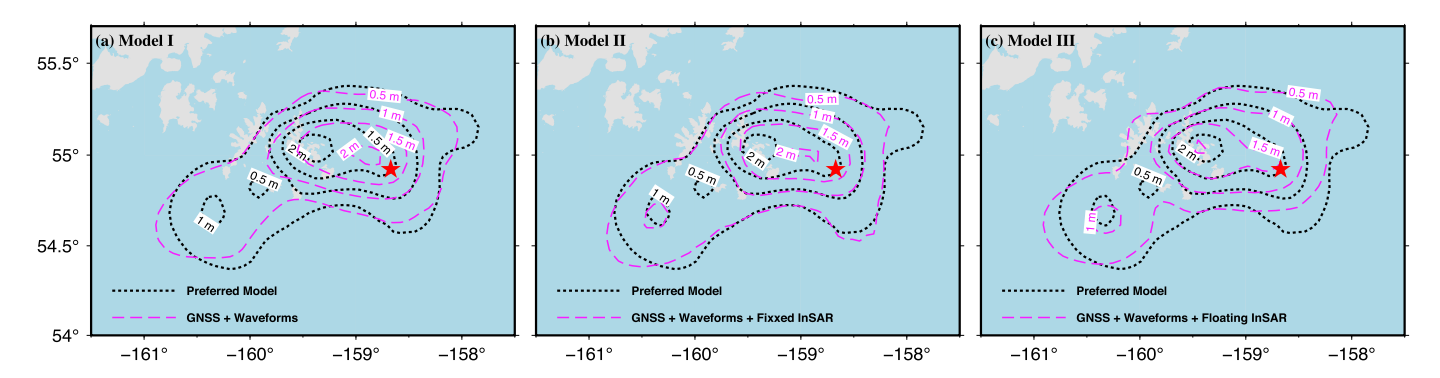


Fig. 5. Comparison of slip model inferred from different data sets (pink contours) compared to our preferred slip model (black contours). (a) Slip distribution inferred from static GNSS, high-rate GNSS and seismic waveforms (Model I). (b) Slip distribution inferred from static GNSS, high-rate GNSS, seismic waveforms and absolute InSAR data (Model II) (c) Slip distribution inferred from static GNSS, high-rate GNSS, seismic waveforms and floating InSAR data (Model III).

quired primarily to reconcile the location of slip constrained by the geodetic data with the timing of slip constrained by the seismic waveforms. Models with a uniform rupture velocity, even when allowing for a spatially variable rise time, could not fit all of the data simultaneously.

4. Discussion

4.1. Contribution of the InSAR data

In this study, the InSAR data are a mix of absolute LOS displacements (islands tied to GNSS sites) and "floating" patches of data that provide relative displacements within the patch. To examine how each subset of the InSAR data contributes to the estimated slip model, we explored model resolution using simulated data sets (Supplemental Text S3 and Fig. S12). The checkerboard resolution tests show that a larger weight given to smoothing would have been required if we did not include the InSAR data. The synthetic checkerboard resolution tests (Fig. S12) show some model artifacts when the InSAR data are excluded, given the hyperparameters for the final preferred model. Model resolution is clearly

lower for models without the InSAR data. Inversion of synthetic data for a slip model that mimics the shape and location of the observed high slip patch (Test III of Fig. S12) shows that the model with InSAR is better able to recover the southwest boundary of the slip patch compared to a model without the InSAR.

We also evaluated alternative inversion models using three different data subsets of the real data to separate the contributions of the floating InSAR data from those of the InSAR data tied to the GNSS sites (Fig. 5). In Model I, we eliminated InSAR observations altogether, using only static GNSS, high-rate GNSS and seismic waveforms to determine the slip pattern (Fig. 5a). Without the InSAR constraints, the peak slip area (slip >2 m) is located closer to the epicenter, not under the Koniuji Islands as in our preferred model. The predicted InSAR phase gradient (Fig. S9) is oriented differently than that observed, showing an anticlockwise rotation especially in the near field. The observed LOS ground displacement on the islands closest to the epicenter are poorly predicted by Model I, with prediction errors exceeding 10 cm on Simeonof Island (Fig. S9f), significantly higher than the \sim 1 cm residuals to our preferred model.

Including the absolute InSAR LOS deformation only (Model II) yields slip details that become more similar to our preferred model (Fig. 5b). The peak slip area shifts slightly towards the Koniuji Islands, the area of >1 m slip becomes more concentrated around the Shumagin Islands, and the high amplitude slip patch (>1 m) west of the Shumagin Islands appears. However, the main slip area is still biased toward the east. The comparison of observed InSAR to the Model II-predicted LOS deformation field (Fig. S10) shows that Model II improves the fit on all GNSS-corrected islands (as these data were used in the inversion), especially on Chernabura Island. The prediction error for Simeonof Island decreased only to \sim 8 cm. The phase gradients (Fig. S10c) are still significantly mismatched for the easternmost, unconstrained islands (Koniuji Islands and Simeonof Island).

Model III (Fig. 5c) uses floating InSAR data (but not the GNSS-tied InSAR). The resulting slip distribution most closely resembles our preferred model, especially in the peak slip region, which is now located under the Koniuji Islands, although the area of slip >2 m remains smaller than in our preferred model (Fig. 5c). The predicted displacements show that these visually slight differences in the slip distribution affect the predicted phase gradients significantly (Fig. S11c) as now the GNSS-tied islands are poorly fit. Notably, Nagai Island, despite being constrained by AC28 GNSS data in the center, shows a remarkable mismatch in phase gradient and LOS fit in its northern part. Likewise, Chernabura Island's southern part drifts toward a misfit of a full phase cycle, despite being constrained at its northern tip by AC12's GNSS data.

Both the relative displacements derived from floating InSAR and absolute displacements from InSAR observations tied to GNSS sites on islands provide important constraints on the slip distribution. The orientation of the InSAR phase gradient is very sensitive to the location of the western edge of the region of high slip. This can be understood by imagining a uniform rectangular rupture are and noting how the magnitudes and orientations of displacement vectors change around the edges of the rupture. The floating InSAR is particularly important as it is the only data from the eastern Shumagin Islands, and its inclusion shows that the maximum slip in the model was below these islands.

4.2. Comparison to different slip models

In addition to our slip model, three other kinematic slip models for the 2020 Simeonof earthquake have been published thus far. While various aspects of a slip model are sensitive to different data types and the chosen inversion method specifics, some characteristics are common across the published models. However, as discussed above and noted below, even apparently slight differences in slip distribution may cause significant changes in the fit to the InSAR data justifying a careful evaluation of all models.

Our model provides the best fit to GNSS offsets among all published models. For example, the largest GNSS horizontal residual reported for the model of Ye et al. (2021) (their Fig. S3) is \sim 3 cm, about 3 times greater than ours and several times the data uncertainty. The RMSE of the static GNSS horizontal and vertical residuals presented for the model of Liu et al. (2020) are about 4.4 mm and 8.7 mm, respectively, which are almost two times larger than ours. Compared to Crowell and Melgar (2020), we have better static GNSS fit at the farther field sites, such as AC40 and AC25 (compare our Fig. S6 to their Fig. 2).

All published models show a unidirectional rupture, propagating westward from the hypocenter, even though different models use different hypocenter locations. The timing of the rupture process is similar across the models, independent of whether teleseismic waveforms, or high-rate GNSS and strong motion waveforms were used. The majority of the moment in various models is released 20–50 s after rupture initiation. Consequently, the

moment-rate function in all models increases sharply $\sim\!20$ s after the mainshock and peaks at $\sim\!30$ s. Among the four models, no significant slip was found shallower than 15 km and large slip was confined between 25 to 45 km (Fig. 6). This may explain the occurrence of only a small tsunami with a maximum wave height of $\sim\!50$ cm.

While the timing of the rupture process is generally similar across the models, the slip pattern, and location and magnitude of slip peaks are more model dependent (and regularization dependent). As high-rate GNSS waveforms are less sensitive to small displacements than broadband seismograph data, the first peak of the moment-rate function at about 10 s after rupture initiation was not reproduced by Crowell and Melgar (2020), although it is present in all models that used seismic data, including ours. The source time functions for all of these models are fairly similar, because the seismic waveform data places strong constraints on the timing of slip, if not always its location.

Another significant difference between various models is the peak slip magnitude and location (Fig. 6). The peak slip we estimated is about 2.2 m at a depth of 35.1 km, which is close to the 2.0 m of Crowell and Melgar (2020), but substantially less than the \sim 3.2 m of Liu et al. (2020) and \sim 3.8 m of Ye et al. (2021). Both of the latter models feature narrower and higher slip peaks compared to the more broadly distributed slip in our model and that of Crowell and Melgar (2020). Different spatial smoothing likely contributes to this difference, but it is the inclusion of the InSAR data in our model that requires a broader region of high slip as opposed to the narrow peaks in some of the models, even when smoothing is decreased (Movie S1). Liu et al. (2020) and Ye et al. (2021) place the peak slip between Nagai Island and the Koniuji islands, with the GNSS sites essentially at the edge of the high slip patch, and then a smaller magnitude slip patch is located further to the west. Liu et al. (2020) put the slip peak slightly to the east of that of Ye et al. (2021), but both of these models have substantial slip west of the Koniuji Islands. In contrast, the highest slip in the model of Crowell and Melgar (2020), using L1-regularization, is focused underneath the Koniuji Islands and Simeonof Island without a westward extension. Our model shows the same, but with a region of significant slip between the hypocenter and the Koniuji Islands.

While Crowell and Melgar (2020), Liu et al. (2020), and Ye et al. (2021), place a patch of higher slip near the hypocenter, all of these models show lower slip between the hypocenter and the eastern Shumagin Islands. Based on a comparison of all the available models, the inclusion of seismic data in the inversion is responsible for the slip patch to the west of the Shumagin Islands, more optimal weighting of GNSS data relative to the waveform data requires the high slip to be located beneath the eastern Shumagin Islands, and the InSAR data further concentrate slip beneath the Koniuji islands. This last point reflects the fact that the InSAR data are not compatible with a western edge of high slip that extends west relative to our preferred model.

4.3. Comparison of coseismic slip, interseismic slip deficit, and slip budget

Generally, large earthquakes are thought to occur in regions of high slip deficit, but the 2020 Simeonof earthquake ruptured within a region of complicated spatial variations in slip deficit, which change systematically along strike (Drooff and Freymueller, 2021; Li and Freymueller, 2018). Interseismic slip deficit rates are high east of the epicenter and decrease to nearly zero (largely creeping) to the west of the Shumagin Islands.

Our relocated hypocenter is located near a sharp along-strike transition in slip deficit rate (Fig. 7a) in the model of Drooff and Freymueller (2021). The western edge of the high slip patch in our

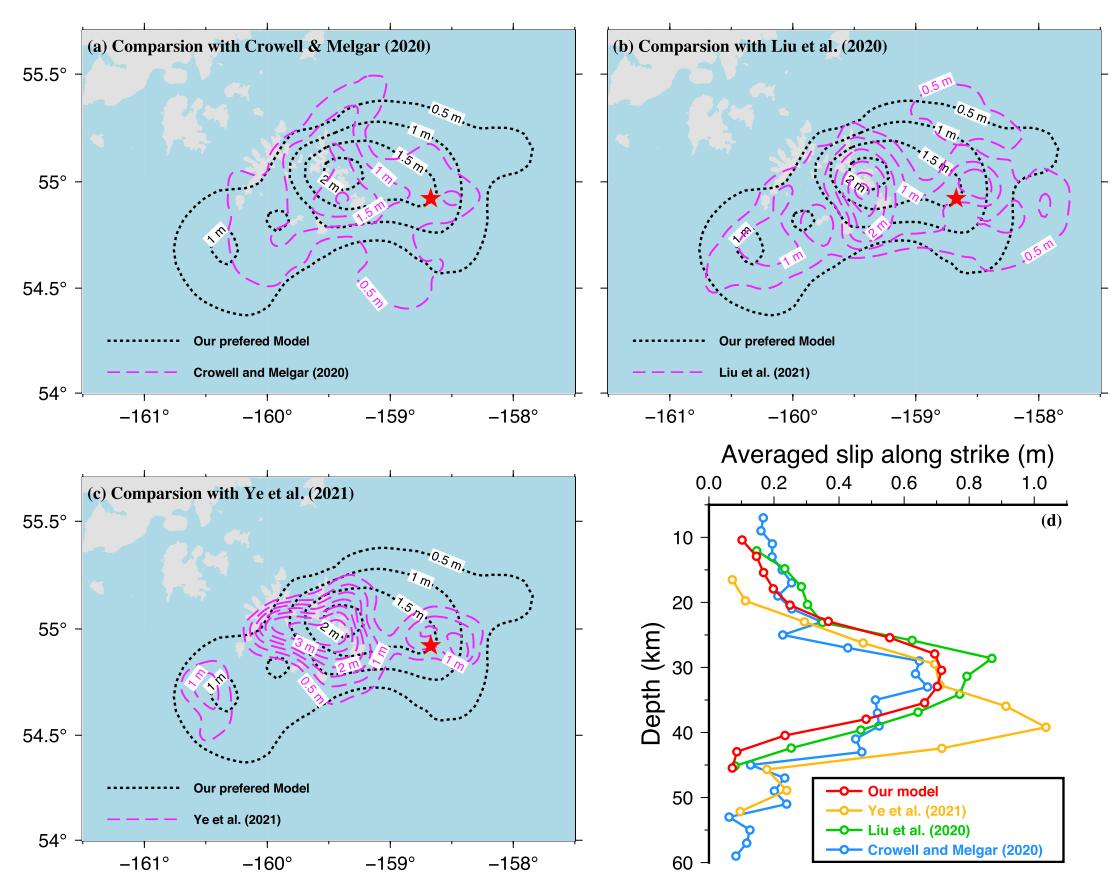


Fig. 6. (a)-(c) Comparison of our slip model to three published models, (d) Averaged slip along strike versus depth of the four slip models.

model closely corresponds to another sharp along-strike transition in slip deficit rate, so the high slip area is almost entirely contained within one segment as inferred from the interseismic deformation (segment 1 in Fig. 7a). The earthquake rupture extended westward of this boundary into the adjacent segment inferred to have a lower slip deficit, but with lower slip. The earthquake may have ruptured the entire width of that segment (segment 2 in Fig. 7).

The published slip deficit models focused primarily on the along-strike segmentation of slip deficit, but the along-dip variation in slip deficit is also critically important, particularly in light of a possible shallow slip deficit and resulting tsunami hazards. All of the published slip models for the 2020 Simeonof earthquake, including ours, agree that no slip occurred shallower than 15 km depth, and little slip was shallower than 20 km (Fig. 6). The coseismic slip was thus released within a region that the interseismic models suggest is only partially coupled.

This motivates our exploration into the relationship between the coseismic slip, the interseismic slip deficit, and the overall subduction interface slip budget and remaining potential seismic hazard for the Shumagin gap, including the consideration of an alternative coupling model. The slip deficit distribution (Drooff and Freymueller, 2021; Li and Freymueller, 2018) is estimated by an inversion of the interseismic GNSS velocities. As with the coseismic inversion, this underdetermined problem requires regularization, which affects the model in areas with poor resolution, especially near the trench (e.g., Schmalzle et al., 2014). In the Shumagin gap region, all GNSS observations are significantly inboard of the trench and sparsely distributed, leading to poor model resolution at shallow depths.

The Drooff and Freymueller (2021) model included an inequality constraint on the slip deficit, which was required to decrease with depth, putting the highest slip deficit at the trench (Fig. 7a). We estimated an alternative model in which the slip deficit values

are assumed to follow a Gaussian distribution with depth instead (hereafter the Gaussian model). We use the same data as Drooff and Freymueller (2021) and adjusted the smoothing to provide a similar fit to the data as their model. The RMSE of the Gaussian model is about 7% higher than that of Drooff and Freymueller (2021). In the Gaussian model, the slip deficit near the trench is fairly low and the maximum slip deficit is centered in the middle depth range, closer to the coseismic slip zone of the 2020 event (Fig. 7b). The slip deficit within the coseismic rupture zone is similar to that of Drooff and Freymueller (2021) (Figs. 7a, 7b). The similarity of the models is due to the tight constraints imposed by the nearby GNSS sites. The maximum slip deficit is shallower than the coseismic slip in both models, suggesting that the plate interface updip of the 2020 rupture is likely more strongly coupled than the part of the interface that slipped during the earthquake. The along-strike segmentation is the same in both models. The largest difference between the models occurs at shallow depths, where the Gaussian model predicts much lower slip deficit values. Combined with our finding of high rupture velocities and slip at intermediate depths, the fact that the data can be adequately fit with low interseismic slip deficits near the trench may help explain the lack of a significant tsunami, as this part may be subject to creep.

In order to assess regional potential seismic hazard after the 2020 Simeonof earthquake, we calculated average slip budgets from 1917 to the present for the two coseismic slip zone segments introduced above. We assumed that coupling values remained constant from 1917 to 2020, and we averaged both slip and slip deficit along strike within each segment (Fig. 7c-f). For both segments, the Gaussian model predicts higher slip deficits than the Drooff and Freymueller (2021) model in the 20–40 km depth range, and thus the remaining slip budget after 2020 is slightly higher, but in both cases and for both segments it is small for depths below 25–30

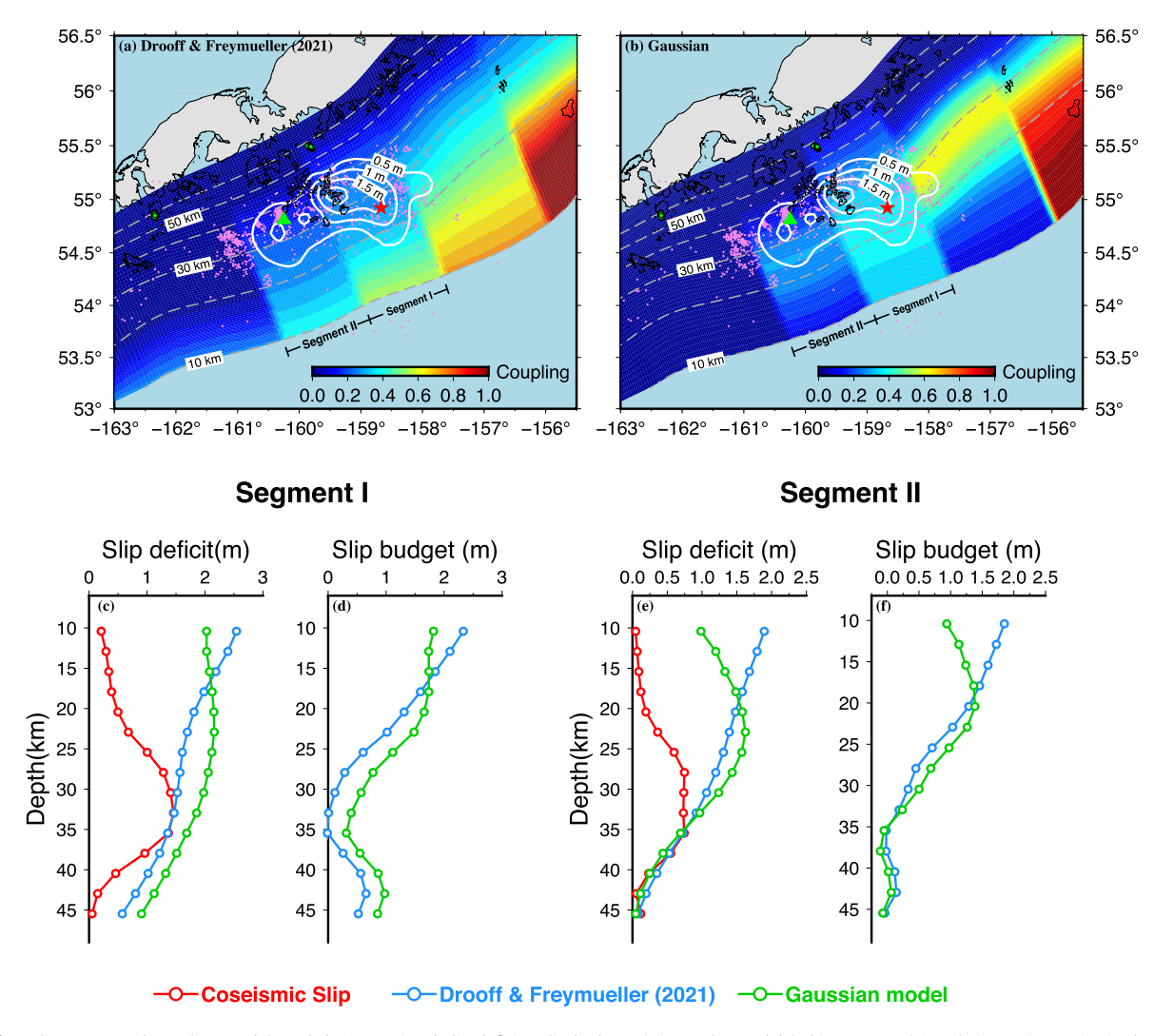


Fig. 7. Differently constrained coupling models and their associated slip deficits, slip budgets. (a) Our slip model (white contours) in relation to interseismic slip coupling of Drooff and Freymueller (2021). In this model, the coupling degrees are assumed to decrease from the trench to the bottom. The solid purple dots show aftershocks ($Mw \ge 2$, USGS) after the mainshock occurrence until Oct. 19, 2020. Green solid dots indicate the low frequency events reported in (Brown et al., 2013). The green triangle indicates the epicenter of the 1993 Ms 6.9 earthquake from (Abers et al., 1995). (b) Our slip model in relation to a Gaussian coupling model. The coupling degrees are assumed to follow a Gaussian distribution, centered at the middle of the slab rather than the top parts. Others are the same as panel (a). (c), (e) are the slip deficits for Segment I and II, respectively (labeled in a, b). The slip coupling degree is assumed to be constant from 1917 to the mainshock occurrence. The interseisic convergence rate we used is 55.60 mm/year for the segment I and 55.9 mm/year for the Segment II (Li et al. 2016). (d), (f) are the slip budgets, the remainder after subtracting our inferred coseismic slip the estimated slip deficits, for Segment I and II, respectively.

km, meaning that the 2020 Simeonof earthquake slip accounted for almost all of the accumulated deep interseismic slip deficit over the previous century. In segment I (eastern Shumagins), where the peak coseismic slip occurred, both models predict $\sim\!\!2$ m of accumulated slip deficit over 1917–2020 in the region that ruptured coseismically, in agreement with our slip model. In both segments the slip deficit profiles from the two interseismic models are quite different at shallow depth, with the Gaussian model predicting 0.5 to 1 m less slip deficit over the last century.

After subtracting the coseismic slip from the cumulative slip deficit, the remaining slip budget is up to ~ 1 m in regions with mainshock coseismic slip larger than 0.5 m in both segments, no matter which interseismic slip deficit distribution is used. This does not consider a Ms 6.9 earthquake that occurred in segment II in 1993, with an average slip of potentially 0.5 m (Beavan, 1993). Hence, the actual slip deficit remaining in segment II will be lower and closer to balance. Most of the cumulative slip deficit has been released between depths of 30 to 40 km. The remaining slip deficit appears unlikely to be able to generate a large event at these depths. As our estimated coseismic rupture extends to the bor-

der of the interseismic creeping regions, we support the conclusion that the Shumagin seismic gap has been almost filled by the 2020 Shumagin earthquake within the depth range of 30–40 km.

Our slip model also confirms that the 2020 Simeonof earthquake did not rupture the shallow part of the megathrust. In the asperity model (Lay and Kanamori, 1981), the extent of large earthquake ruptures depends on the size and spacing of asperities on the fault plane, their pre-existing stress state, and dynamic stresses associated with the fault rupture (e.g., Brandes and Tanner, 2020; Corbi et al., 2017; Scholz, 2019). Larger and more homogeneous asperities may require a larger shear stress to fail. Asperities that are pushed beyond the failure point by the static and dynamic rupture stresses become part of the rupture zone, while asperities that do not fail become barriers to further rupture. Although we cannot rule out an interseismic slip deficit distribution without any partially locked part shallower than the Simeonof earthquake rupture, two different model regularizations both suggest that there is an updip locked region that did not rupture in 2020. Thus, future large shallow earthquakes must be considered possible, and the 2020 Simeonof earthquake increased stresses on this presumed shallow locked patch.

There have been several recent examples of large earthquakes that ruptured only at depth, similar to the Simeonof event. The 2015 Gorkha (Nepal) earthquake ruptured only the deeper part of the locked zone of the Himalayan megathrust (Elliott et al., 2016; Wang and Fialko, 2015). Postseismic studies confirm that no shallow afterslip followed the earthquake, consistent with a remaining un-ruptured high-strength asperity (e.g., Mencin et al., 2016; Tian et al., 2020). The 2007 M8.4 Mentawai, Sumatra earthquake (Konca et al., 2008) was followed in 2010 by an M7.8 earthquake that ruptured only at shallow depth (e.g., Hill et al., 2012). This latter event pair indicates that a shallow asperity may fail to rupture even when the earlier event brings it very close to failure.

Assuming the Drooff and Freymueller (2021) model, the accumulated slip deficit near the trench is up to 2.3 m in Segment I and 1.8 m in Segment II. Regardless of the interseismic model, the slip budget remains large enough for another Mw \sim 7.8 event to occur at depths shallower than 25 km if it ruptured across both segments. This indicates that the seismic and tsunami hazards may remain high after the 2020 Simeonof event. Even though the slip budgets near the trench are much smaller in the Gaussian model than those predicted by Drooff and Freymueller (2021), \sim 2.0 m compared to \sim 2.5 m for Segment I and \sim 0.9 m compared to \sim 1.9 for Segment II, the Gaussian model predicts higher slip budgets in from 17 to 25 km. Ultimately, resolution of the seismic potential of the accretionary toe portion of the Shumagin gap will require additional constraints from seafloor geodetic observations.

An alternative to a M7+ earthquake would be for the accumulated slip deficit to be partially or fully accommodated through slow-slip events. Shallow, near-trench slow-slip events have been documented along several margins including New Zealand (Wallace et al., 2016), Japan (Yamashita et al., 2015), and Ecuador (Vallée et al., 2013), usually in segments where the interface is mostly creeping or highly heterogeneous (Araki et al., 2017). The Shumagin segment has a heterogeneous plate interface (Bécel et al., 2017) and appears to have low coupling based on onshore geodetic data (Drooff and Freymueller, 2021), but the lack of offshore data prevents resolution of shallow transient events. To date no such events have been reported from this region, although a small transient event suspected to be under the Shumagin Islands was reported in the supplement of Li and Freymueller (2018).

5. Conclusions

We examine the rupture process of the 2020 Simeonof earthquake using a combination of static GNSS displacements, high-rate GNSS-inferred and global seismic waveforms, and InSAR LOS deformation. The rupture was unidirectional, propagating westward during 130 s with an average rupture velocity of \sim 1.9 km/s. Coseismic slip was focused below and east of Big and Little Koniuji Islands and mostly occurred between 20 s to 50 s after the rupture initiation. The InSAR observations, especially the floating In-SAR data on near-field islands, are essential to constrain the slip distribution. Two alternative plate interface coupling models suggest that the slip deficit in the 30-40 km depth range has been mostly balanced. However, both models suggest some remaining shallow slip deficit in the poorly constrained shallow portion of the interface, suggesting significant remaining seismic risk in the accretionary toe portion in the Shumagin gap, that requires neartrench geodetic observations to assess.

CRediT authorship contribution statement

ZX performed tele-seismic waveforms processing and finite-fault inversion; RG and LF conducted InSAR, high-rate GNSS data

processing; JF performed the static GNSS data processing; CD prepared the alternative slip deficit models; JF, RG and JE conceived the project, and along with ZX interpreted the results and wrote the manuscript collaboratively.

Declaration of competing interest

The authors declare that they have no known competing financial interests or personal relationships that could have appeared to influence the work reported in this paper.

Data availability

Global seismic waveforms are downloaded from the Incorporated Research Institutions for Seismology (IRIS) Wilber 3 System (http://ds.iris.edu/wilber3/find_event) and included data from the following seismic networks: (1) the G (GEOSCOPE; IPGP/EOST); (2) the IC (NCDSN; ASL/USGS, 1992); (3) the IM; (4) the IU (GSN; IRIS/USGS, 1988); (5) the MN (MetNet; INGV, 1990); (6) the CI (SCSN; Caltech/USGS, 1926); (7) the CN (CNSN; NRCAN, 1975); (8) the II (GSN; IRIS/IDA, 1986); (9) the GE (GEOFON; GFZ-Potsdam, 1991); and (10) the HK. References and DOIs for the data are listed in Table S3.

Raw GNSS data used in this study are available at the GAGE Facility archive, operated by UNAVCO (http://www.unavco.org) or through the National Geodetic Survey (https://geodesy.noaa.gov/CORS/). References and DOIs for the data are listed in Table S3. InSAR results were derived from Copernicus Sentinel data (2020), which is further described in Torres et al. (2012). SAR data were retrieved from the ASF DAAC, processed by ESA.

The background seismicity catalog was downloaded from the ISC (https://www.isc.ac.uk/). The aftershock catalog was downloaded from USGS (https://earthquake.usgs.gov/earthquakes/map/). The model files generated in this study are available at the Figshare website (https://doi.org/10.6084/m9.figshare.16567470.v1 for free public access).

Acknowledgements

Some of this material is based on services provided by the GAGE Facility, operated by UNAVCO, Inc., with support from the National Science Foundation and the National Aeronautics and Space Administration under NSF Cooperative Agreement EAR-1724794

The facilities of IRIS Data Services, and specifically the IRIS Data Management Center, were used for access to waveforms, related metadata, and/or derived products used in this study. IRIS Data Services are funded through the Seismological Facilities for the Advancement of Geoscience (SAGE) Award of the National Science Foundation under Cooperative Support Agreement EAR-1851048.

This research was supported by the Science Fund for Creative Research Groups of the National Natural Science Foundation of China (Nos. 41721003) and National Key Research and Development Plan of China (Nos. 2018YFC1503605) to Wuhan University (ZX) and National Science Foundation awards EAR-2052558 to Michigan State University (JF and JE) and EAR-2052569 to the University of Alaska Fairbanks (RG and LF), and the Geology of Solid Earth Endowment at Michigan State. ZX's study period at Michigan State University was supported by the China Scholarship Council (201906270173).

We thank Angelyn Moore at JPL for help in setting up the high-rate GNSS processing with GipsyX. We appreciate Dr. Brendan Crowell, Dr. Lingling Ye, and Dr. Chengli Liu for providing their coseismic slip models shown in Fig. 6. All Figures are made with Generic Mapping Tools (Wessel et al., 2019)

Appendix A. Supplementary material

Supplementary material related to this article can be found online at https://doi.org/10.1016/j.epsl.2021.117241.

References

- Abers, G.A., Beavan, J., Horton, S., Jaumé, S., Triep, E., 1995. Large accelerations and tectonic setting of the May 1993 Shumagin Islands earthquake sequence. Bulletin of the Seismological Society of America 85 (6), 1730–1738.
- Araki, E., Saffer, D.M., Kopf, A.J., Wallace, L.M., Kimura, T., Machida, Y., Ide, S., Davis, E., 2017, IODP Expedition 365 shipboard scientists. Science 365 (6343), 1157–1160
- Argus, D.F., Gordon, R.G., Heflin, M.B., Ma, C., Eanes, R.J., Willis, P., et al., 2010. The angular velocities of the plates and the velocity of Earth's centre from space geodesy. Geophys. J. Int. 180 (3), 913–960. https://doi.org/10.1111/j.1365-246X. 2009.04463 x
- Aster, R.C., Borchers, B., Thurber, C.H., 2018. Chapter six Iterative methods. In: Aster, R.C., Borchers, B., Thurber, C.H. (Eds.), Parameter Estimation and Inverse Problems, third edition. Elsevier, pp. 151–180.
- Bécel, A., Shillington, D.J., Delescluse, M., Nedimović, M.R., Abers, G.A., Saffer, D.M., Webb, S.C., Keranen, K.M., Roche, P.H., Li, J., Kuehn, H., 2017. Tsunamigenic structures in a creeping section of the Alaska subduction zone. Nat. Geosci. 10 (8), 609–613
- Bertiger, W., Bar-Sever, Y., Dorsey, A., Haines, B., Harvey, N., Hemberger, D., et al., 2020. GipsyX/RTGx, a new tool set for space geodetic operations and research. Adv. Space Res. 66 (3), 469–489. https://doi.org/10.1016/j.asr.2020.04.015.
- Brandes, C., Tanner, D.C., 2020. Chapter 2 Fault mechanics and earthquakes. In: Tanner, D., Brandes, C. (Eds.), Understanding Faults. Elsevier, pp. 11–80.
- Brown, J.R., Prejean, S.G., Beroza, G.C., Gomberg, J.S., Haeussler, P.J., 2013. Deep low-frequency earthquakes in tectonic tremor along the Alaska-Aleutian subduction zone. J. Geophys. Res., Solid Earth 118 (3), 1079–1090. https://doi.org/10.1029/2012/B009459.
- Chen, C.W., Zebker, H.A., 2002. Phase unwrapping for large SAR interferograms: statistical segmentation and generalized network models. IEEE Trans. Geosci. Remote Sens. 40 (8), 1709–1719. https://doi.org/10.1109/TGRS.2002.802453.
- Corbi, F., Funiciello, F., Brizzi, S., Lallemand, S., Rosenau, M., 2017. Control of asperities size and spacing on seismic behavior of subduction megathrusts. Geophys. Res. Lett. 44 (16), 8227–8235. https://doi.org/10.1002/2017GL074182.
- Crowell, B.W., Melgar, D., 2020. Slipping the Shumagin gap: a kinematic coseismic and early afterslip model of the Mw 7.8 Simeonof Island, Alaska, Earthquake. Geophys. Res. Lett. 47. https://doi.org/10.1029/2020GL090308.
- Davies, J., Sykes, L., House, L., Jacob, K., 1981. Shumagin seismic gap, Alaska Peninsula: history of great earthquakes, tectonic setting, and evidence for high seismic potential. J. Geophys. Res., Solid Earth 86 (B5), 3821–3855. https://doi.org/10.1029/JB086iB05p03821.
- Drooff, C., Freymueller, J.T., 2021. New constraints on slip deficit on the Aleutian megathrust and inflation at Mt. Veniaminof, Alaska from repeat GPS measurements. Geophys. Res. Lett. 48 (4). https://doi.org/10.1029/2020GL091787.
- Elliott, J.R., Jolivet, R., González, P.J., Avouac, J.-P., Hollingsworth, J., Searle, M.P., Stevens, V.L., 2016. Himalayan megathrust geometry and relation to topography revealed by the Gorkha earthquake. Nat. Geosci. 9 (2), 174–180. https:// doi.org/10.1038/ngeo2623.
- Estabrook, C.H., Boyd, T.M., 1992. The Shumagin Islands, Alaska, earthquake of 31 May 1917. Bull. Seismol. Soc. Am. 82 (2), 755–773.
- Font, Y., Segovia, M., Vaca, S., Theunissen, T., 2013. Seismicity patterns along the Ecuadorian subduction zone: new constraints from earthquake location in a 3-D a priori velocity model. Geophys. J. Int. 193, 263–286. https://doi.org/10.1093/gji/ggs083.
- Hayes, G.P., Moore, G.L., Portner, D.E., Hearne, M., Flamme, H., Furtney, M., Smoczyk, G.M., 2018. Slab2, a comprehensive subduction zone geometry model. Science 362 (6410), 58–61. https://doi.org/10.1126/science.aat4723.
- Herman, M.W., Furlong, K.P., 2021. Triggering an unexpected earthquake in an uncoupled subduction zone. Sci. Adv. 7 (13), eabf7590. https://doi.org/10.1126/sciadv.abf7590
- Hill, E.M., Borrero, J.C., Huang, Z., Qiu, Q., Banerjee, P., Natawidjaja, D.H., et al., 2012. The 2010 Mw 7.8 Mentawai earthquake: very shallow source of a rare tsunami earthquake determined from tsunami field survey and near-field GPS data. J. Geophys. Res., Solid Earth 117 (B6). https://doi.org/10.1029/2012JB009159.
- Ji, C., Wald, D.J., Helmberger, D.V., 2002. Source description of the 1999 hector mine, California, earthquake, Part I: wavelet domain inversion theory and res-

- olution analysis. Bull. Seismol. Soc. Am. 92 (4), 1192–1207. https://doi.org/10. 1785/0120000916.
- Ji, C., Helmberger, D.V., Wald, D.J., Ma, K.-F., 2003. Slip history and dynamic implications of the 1999 Chi-Chi, Taiwan, earthquake. J. Geophys. Res. 108 (B9). https:// doi.org/10.1029/2002JB001764.
- Konca, A.O., Avouac, J.-P., Sladen, A., Meltzner, A.J., Sieh, K., Fang, P., et al., 2008. Partial rupture of a locked patch of the Sumatra megathrust during the 2007 earthquake sequence. Nature 456 (7222), 631–635. https://doi.org/10.1038/nature07572.
- Lay, T., Kanamori, H., 1981. An asperity model of large earthquake sequences. In: Simpson, D.W., Richards, P.G. (Eds.), Earthquake Prediction.
- Li, S., Freymueller, J.T., 2018. Spatial variation of slip behavior beneath the Alaska peninsula along Alaska-Aleutian subduction zone. Geophys. Res. Lett. 45 (8), 3453–3460. https://doi.org/10.1002/2017gl076761.
- Li, S., Freymueller, J., McCaffrey, R., 2016. Slow slip events and time-dependent variations in locking beneath lower cook inlet of the Alaska-Aleutian subduction zone. J. Geophys. Res., Solid Earth 121 (2), 1060–1079. https://doi.org/10.1002/2015JB012491.
- Liu, C., Lay, T., Xiong, X., Wen, Y., 2020. Rupture of the 2020 Mw 7.8 earthquake in the Shumagin gap inferred from seismic and geodetic observations. Geophys. Res. Lett. 47 (22). https://doi.org/10.1029/2020GL090806.
- Mencin, D., Bendick, R., Upreti, B.N., Adhikari, D.P., Gajurel, A.P., Bhattarai, R.R., et al., 2016. Himalayan strain reservoir inferred from limited afterslip following the Gorkha earthquake. Nat. Geosci. 9 (7), 533–537. https://doi.org/10.1038/ngeo2734.
- Pasyanos, M.E., Masters, T.G., Laske, G., Ma, Z., 2014. LITHO1.0: an updated crust and lithospheric model of the Earth. J. Geophys. Res., Solid Earth 119 (3), 2153–2173. https://doi.org/10.1002/2013JB010626.
- Sandwell, D., Mellors, R., Tong, X., Wei, M., Wessel, P., 2011. Open radar interferometry software for mapping surface deformation. Eos Trans. AGU 92 (28), 234. https://doi.org/10.1029/2011EO280002.
- Schmalzle, G.M., McCaffrey, R., Creager, K.C., 2014. Central Cascadia subduction zone creep. Geochem. Geophys. Geosyst. 15 (4), 1515–1532. https://doi.org/10.1002/2013GC005172.
- Scholz, C.H., 2019. The Mechanics of Earthquakes and Faulting, 3rd ed. Cambridge University Press, Cambridge.
- Shao, G., Li, X., Ji, C., Maeda, T., 2011. Focal mechanism and slip history of the 2011 Mw 9.1 off the Pacific coast of Tohoku earthquake, constrained with teleseismic body and surface waves. Earth Planets Space 63 (7), 559–564. https://doi.org/10.5047/eps.2011.06.028.
- Storchak, D.A., Harris, J., Brown, L., Lieser, K., Shumba, B., Di Giacomo, D., 2020. Rebuild of the bulletin of the international seismological centre (ISC)—part 2: 1980–2010. Geosci. Lett. 7 (1), 18. https://doi.org/10.1186/s40562-020-00164-6.
- Tian, Z., Freymueller, J.T., Yang, Z., 2020. Spatio-temporal variations of afterslip and viscoelastic relaxation following the Mw 7.8 Gorkha (Nepal) earthquake. Earth Planet. Sci. Lett. 532, 116031. https://doi.org/10.1016/j.epsl.2019.116031.
- Torres, R., Snoeij, P., Geudtner, D., Bibby, D., Davidson, M., Attema, E., et al., 2012. GMES Sentinel-1 mission. The Sentinel Missions - New Opportunities for Science, Remote Sens. Environ. 120, 9–24. https://doi.org/10.1016/j.rse.2011.05.028.
- Vallée, M., Nocquet, J.-M., Battaglia, J., Font, Y., Segovia, M., Régnier, M., Mothes, P., Jarrin, P., Cisneros, D., Vaca, S., Yepes, H., Martin, X., Béthoux, N., Chlieh, M., 2013. Intense interface seismicity triggered by a shallow slow slip event in the Central Ecuador subduction zone. J. Geophys. Res. 118, 2965–2981.
- Wallace, L.M., Webb, S.C., Ito, Y., Mochizuki, K., Hino, R., Henrys, S., Schwartz, S.Y., Sheehan, A.F., 2016. Slow slip near the trench at the Hikurangi subduction zone. Science 352 (6286), 701–704.
- Wang, K., Fialko, Y., 2015. Slip model of the 2015 Mw 7.8 Gorkha (Nepal) earthquake from inversions of ALOS-2 and GPS data. Geophys. Res. Lett. 42 (18), 7452–7458. https://doi.org/10.1002/2015GL065201.
- Wessel, P., Luis, J.F., Uieda, L., Scharroo, R., Wobbe, F., Smith, W.H.F., Tian, D., 2019. The generic mapping tools version 6. Geochem. Geophys. Geosyst. 20 (11), 5556–5564. https://doi.org/10.1029/2019GC008515.
- Yamashita, Y., Yakiwara, H., Asano, Y., Shimizu, H., Uchida, K., Hirano, S., Umakoshi, K., Miyamachi, H., Nakamoto, M., Fukui, M., Kamizono, M., Kanehara, H., Yamada, T., Shinohara, M., Obara, K., 2015. Migrating tremor off southern Kyushu as evidence for slow slip of a shallow subduction interface. Science 348, 676–679. https://doi.org/10.1126/science.aaa4242pmid:25954006.
- Ye, L., Lay, T., Kanamori, H., Yamazaki, Y., Cheung, K.F., 2021. The 22 July 2020 MW 7.8 Shumagin seismic gap earthquake: partial rupture of a weakly coupled megathrust. Earth Planet. Sci. Lett. 562, 116879. https://doi.org/10.1016/j. epsl.2021.116879.